Eur. Phys. J. A (2006)
DOI 10.1140/epja/i2005-10237-5

THE EUROPEAN PHYSICAL JOURNAL A

Potential energy surfaces and penetrabilities for sub-barrier synthesis of Z = 118 isotopes

R.A. Gherghescu[1,a], W. Greiner[2], and S. Hofmann[3]

[1] Horia Hulubei - National Institute for Nuclear Physics and Engineering, P.O. Box MG-6, RO-76900 Bucharest, Romania
[2] Frankfurt Institute for Advanced Studies, J.W. Goethe Universitaet, D-60438 Frankfurt am Main, Germany
[3] Gesellschaft für Schwerionenforschung, Planckstrasse 1, D-64291 Darmstadt, Germany

Received: 16 December 2005 / Revised version: 26 January 2006 /
Published online: 23 February 2006 – © Società Italiana di Fisica / Springer-Verlag 2006
Communicated by G.A. Orlandini

Abstract. A specialized macroscopic-microscopic method is applied to calculate binary configuration deformation energy for fusion processes. The deformed two-center shell model is utilized to obtain the transition of the two independent level schemes for target and projectile, going through overlapping configuration up to the final compound nucleus. The macroscopic part is obtained with the usual Yuakawa-plus-exponential method applied to fusion-like configuration. The tensor of inertia is obtained within the Werner-Wheeler approach and dynamics is treated using the multidimensional WKB penetrability method. Calculations are applied to the sub-barrier synthesis of $^{294,290,286,280}118$ isotopes.

PACS. 21.10.Pc Single-particle levels and strength functions – 21.60.Cs Shell model – 25.70.Jj Fusion and fusion-fission reactions

1 Introduction

Potential energy surfaces usually exhibit valleys interpreted as favourable paths towards complete fusion. Such valleys appear especially as a consequence of shell corrections, when proton and/or neutron magicity are present in reaction partners, thus being associated with spherical nuclei. The role of N/Z ratio has also been analyzed [1]. When deformation is introduced, new valleys are displayed as a result of deformed closed shells of the target or projectile. Such valleys can also provide low-energy lanes for the use of sub-barrier fusion reactions. Studies of potential energy surfaces have been performed within the framework of self-consistent nuclear models like Skyrme-Hartree-Fock and relativistic mean field [2,3]. In these articles it is demonstrated that shell closures lower the fusion barrier for a given projectile - (A_P, Z_P) and target - (A_T, Z_T) pair, when cold fusion reactions are considered. The same closure effect is stressed also in a cluster emission type calculation [4]. Sub-barrier fusion reactions have low cross-section values, but the final compound nucleus could be reached in a more stable point, close to the ground state. When dynamics is studied introducing the influence of the mass tensor, some pairs of target-projectile can be chosen following the criteria of highest penetrability value. For every given mass asymmetry, the optimal (Z_T, Z_P) charge division has to be found. If one choose a neutron-richer isotope as a projectile, an important change in the cross-section value occurs [1]. One has information about the evolution of mass-charge combinations in fusion reactions from diffusion-type calculations [5], where intermediate equilibrium N/Z-values are obtained. This work aims as a first step, to the calculation of the potential energy surfaces for four superheavy isotopes: $^{294,290,286,280}118$. The multidimensional space of deformation shall be reduced to (R, η_A), where R is the distance between centers and $\eta_A = (A_T - A_P)/A$ is the mass asymmetry for fusion-like configurations. The second step is the penetrability calculation, which implies the introduction of the mass tensor and the computation of the WKB penetrability with help of the action integral, for the four superheavy nuclei mentioned above. In sect. 2 the space of deformation and the energy calculation is presented. Dynamics and tensor calculation are treated in sect. 3 and the results are discussed in sect. 4.

2 Binary macroscopic-microscopic method

Fusion-like configurations are used for the total deformation energy calculation, and a typical shape is displayed in fig. 1, where b_T, a_T and b_P, a_P are the small and large semiaxes of the target and projectile respectively, z_s is the

[a] e-mail: rgherg@ifin.nipne.ro

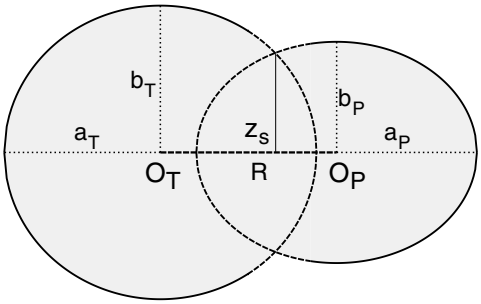

Fig. 1. Typical fusion configuration for spheroidally deformed target and projectile in head-on collisions.

position of the separation plane and R is the distance between centers. All these geometrical parameters form the space of deformation, and furtheron one shall work with: $\chi_T = b_T/a_T$, $\chi_P = b_P/a_P$, b_P and R as degrees of freedom, so that the surface function is defined as

$$\rho_s^2 = \rho_s^2(b_P, \chi_T, \chi_P, R; z) \tag{1}$$

in cylindrical coordinates. The boundary conditions for χ_T and χ_P are

$$\begin{aligned} \chi_T(R_t) &= \chi_T^{(0)}, \\ \chi_P(R_t) &= \chi_P^{(0)}, \\ \chi_T(R_f) &= \chi_{CN}, \end{aligned} \tag{2}$$

where R_t is the touching-point distance between centers, R_f is the final distance when the projectile is completely embedded into the target, $\chi_T^{(0)}$, $\chi_P^{(0)}$ and χ_{CN} are the initial deformations of the target, projectile and compound nucleus, respectively. In between these values, the variation of the parameters is independent. When taking the projectile volume to decrease with a given volume quanta ΔV at every step with fixed R, the small semiaxis b_P becomes a function as

$$b_P = b_P(b_0, b_P^0; \Delta V, V_P; R), \tag{3}$$

where b_0 and b_P^0 are the semiaxis of the compound nucleus and projectile, respectively, and V_P is the initial volume of the projectile. Also b_P depends, at every R, on the intermediary values of χ_T and χ_P. This work proposes two laws of variation for the target and projectile semiaxis ratios, so as to fulfill the boundary conditions:

$$\chi_T = \chi_T^{(0)} + (\chi_{CN} - \chi_T^{(0)}) \exp\left[-\left(\frac{R - R_f}{R - R_t} \kappa_{\chi T} \right)^2 \right] \tag{4}$$

which insures $\chi_T = \chi_T^{(0)}$ for $R = R_t$ and finally $\chi_T = \chi_{CN}$ for $R = R_f$ (complete overlapping). For the projectile

$$\chi_P = \chi_P^{(0)} + (\chi_P^{(f)} - \chi_P^{(0)}) \exp\left[-\left(\frac{R - R_f}{R - R_t} \kappa_{\chi P} \right)^2 \right], \tag{5}$$

where

$$\chi_P^{(f)} = \chi_P^{(0)} + \frac{\kappa_{i2}}{10}(\chi_{CN} - \chi_P^{(0)}) \tag{6}$$

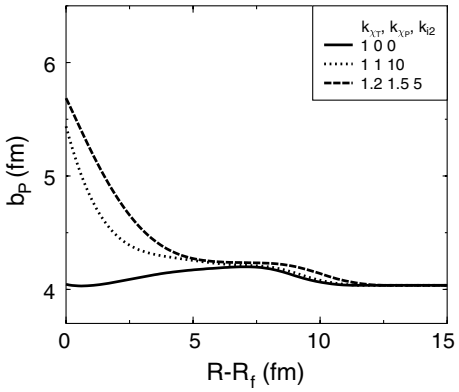

Fig. 2. Different paths of variation for the small semiaxis of the projectile (b_P) as a function of R for three different sets of variable values (see text and eqs. (14) and (15)).

is the final deformation of the completely embedded projectile. Note that κ_{i2} is arbitrary and introduces a new degree of freedom, the final value of the projectile semiaxis ratio as taking any value between the initial projectile and final synthesized nucleus value. Equations (3), (4) and (5) define the geometrical parameters as functions of numerical variables $\kappa_{\chi T}$, $\kappa_{\chi P}$ and κ_{i2}, so that

$$\begin{aligned} b_P &= b_P(\kappa_{i2}, \kappa_{\chi T}, \kappa_{\chi P}; R), \\ \chi_T &= \chi_T(\kappa_{i2}, \kappa_{\chi T}, \kappa_{\chi P}; R), \\ \chi_P &= \chi_P(\kappa_{i2}, \kappa_{\chi T}, \kappa_{\chi P}; R). \end{aligned} \tag{7}$$

As an example, fig. 2 displays the variation of the small semiaxis of the projectile, b_P, with the distance between centers during the overlapping process, for three sets of the above-mentioned numerical parameters. Within the allowed range of variation of the degrees of freedom, a specialized binary macroscopic-microscopic method is used to calculate the deformation energy. The microscopic part is calculated with the deformed two-center shell model [6]. In the Schrödinger equation

$$H\Psi - E\Psi = 0, \tag{8}$$

the total Hamiltonian

$$H = -\frac{\hbar}{2m_0}\Delta + V(\rho, z) + V_{\Omega s} + V_{\Omega^2} \tag{9}$$

is deformation dependent. The deformed two-center oscillator potential for target and projectile regions v_T and v_P reads

$$V(\rho, z) = \begin{cases} V_T(\rho, z) = \frac{1}{2} m_0 \omega_{\rho_T}^2 \rho^2 + \frac{1}{2} m_0 \omega_{z_T}^2 (z + z_T)^2 \ , \text{for } v_T, \\ V_P(\rho, z) = \frac{1}{2} m_0 \omega_{\rho_P}^2 \rho^2 + \frac{1}{2} m_0 \omega_{z_P}^2 (z - z_P)^2 \ , \text{for } v_P, \end{cases} \tag{10}$$

where z_T and z_P are the centers of the target and projectile, and equality

$$V_T(\rho, z) = V_P(\rho, z) \tag{11}$$

defines the border between v_T and v_P regions where the two potentials are active. The deformation dependence is contained in the relations between frequencies and semiaxes

$$\begin{aligned} m_0\omega_{\rho_i}^2 &= (a_i/b_i)^{2/3}\cdot m_0\omega_{0i}^2 = (a_i/b_i)^{2/3}\cdot 54.5/R_i^2, \\ m_0\omega_{zi}^2 &= (b_i/a_i)^{4/3}\cdot m_0\omega_{0i}^2 = (b_i/a_i)^{4/3}\cdot 54.5/R_i^2, \end{aligned} \tag{12}$$

where $R_i = r_0 A_i^{1/3}$, and b_i, a_i are the spheroid semiaxes. Angular-momentum–dependent potentials, $V_{\Omega s}$ and V_{Ω^2} are constructed to comply to the $V(\rho, z)$-dependence and hermicity of the operators, so that

$$V_{so} = \begin{cases} -\left\{ \dfrac{\hbar}{m_0\omega_{0T}}\kappa_T(\rho,z), (\nabla V^{(r)}\times\mathbf{p})\mathbf{s} \right\}, & v_T\text{-region}, \\ -\left\{ \dfrac{\hbar}{m_0\omega_{0P}}\kappa_P(\rho,z), (\nabla V^{(r)}\times\mathbf{p})\mathbf{s} \right\}, & v_P\text{-region}, \end{cases} \tag{13}$$

and

$$V_{\mathbf{l}^2} = \begin{cases} -\left\{ \dfrac{\hbar}{m_0^2\omega_{0T}^3}\kappa_T\mu_T(\rho,z), (\nabla V\times\mathbf{p})^2 \right\}, & v_T\text{-region}, \\ -\left\{ \dfrac{\hbar}{m_0^2\omega_{0P}^3}\kappa_P\mu_P(\rho,z), (\nabla V\times\mathbf{p})^2 \right\}, & v_P\text{-region}. \end{cases} \tag{14}$$

In such a way the spin-orbit term follows any changes in the deformation of the partially overlapped fragments. The matrix diagonalization of H generates the level scheme of the fusion configuration, for spheroidally deformed nuclei, at any given distance R between centers and intermediary independent b_P, χ_T and χ_P. The level scheme sequence from the touching point up to complete overlapping is input data for the Strutinsky method [7], and calculations are performed separately for protons and neutrons. Since superheavy nuclei survive mainly due to negative shell corrections, their macroscopic barrier being negligible [8], this step of the algorithm is crucial to the study of sub-barrier fusion reactions. One expects that at certain intermediary deformations, partially overlapped nuclear shells display deformed proton and/or neutron closures and such minima are generated in the shell corrections. Shell corrections minimum sequences have the main role in generating energy valleys on potential energy surfaces (PES).

The macroscopic part is obtained using the Yukawa-plus-exponential method, specialized to binary processes. The Coulomb term E_C [9] and the nuclear surface term E_Y [10] are computed as

$$E_C = \frac{2\pi}{3}(\rho_{eT}^2 F_{C_T} + \rho_{eP}^2 F_{C_P} + 2\rho_{eT}\rho_{eP}F_{C_{TP}}), \tag{15}$$

and

$$E_Y = \frac{1}{4\pi r_0^2}[c_{sT}F_{EYT} + c_{sP}F_{EY_P} + 2(c_{sT}c_{sP})^{1/2}F_{EY_{TP}}], \tag{16}$$

where ρ_{ei} is the charge density and c_{si} the surface coefficient. F_{C_i} and F_{EY_i} are shape-dependent integrals. The peculiarity resides in the last term in both formulas, $F_{C_{TP}}$ and $F_{EY_{TP}}$, which account for the interaction between non-overlapped parts of the overlapping configuration. Details about these terms are given in [11,12].

The total deformation-dependent macroscopic energy is calculated as the sum of the Coulomb and surface terms:

$$E_{macro} = (E_C - E_C^{(0)}) + (E_Y - E_Y^{(0)}), \tag{17}$$

where $E_C^{(0)}$ and $E_Y^{(0)}$ are the values for the corresponding spherical compound nucleus. Finally, the deformation energy is computed as the sum of the macroscopic part and the shell correction:

$$E_{def} = E_{macro} + E_{shell}. \tag{18}$$

3 Dynamics

In order to obtain the penetrabilities for different reaction channels, the action integral must be computed. Besides the usual deformation energy, the nuclear inertia tensor, which accounts for the reaction of the nucleus to the deformation along a given degree of freedom, is to be computed. This work uses the Werner-Wheeler approach to obtain the mass tensor components within the four-dimensional space of (b_P, χ_T, χ_P, R). In cylindrical coordinates these components read [13]

$$B'_{ij} = \int_{z_m}^{z_M} T_{ij}(z;q)\mathrm{d}z, \tag{19}$$

where

$$T_{ij}(z,q) = \rho_s^2(z,q)\left[X_iX_j + \frac{1}{8}\rho_s^2(z,q)\frac{\partial X_i}{\partial z}\frac{\partial X_j}{\partial z}\right]. \tag{20}$$

The q set accounts for any of the four independent variables describing the shape, together with the surface function $\rho_s^2(z,q)$, where X_i are also shape dependent:

$$X_i(z) = \frac{1}{\rho_s^2(z;q)}\frac{\partial}{\partial q_i}\int_z^{z_M}\rho_s^2(z';q)\mathrm{d}z'. \tag{21}$$

The formulas for the tensor components are developed with the center of the target as origin, which does not correspond to the center of mass of the system. If one starts with the kinetic energy in a discrete mass body:

$$\sum_{i,j} m_i m_j \dot{\mathbf{r}}'_i\dot{\mathbf{r}}'_j = \sum_{i,j} m_i m_j \dot{\rho}'_i\dot{\rho}'_j + \sum_{i,j} m_i m_j \dot{z}'_i\dot{z}'_j \tag{22}$$

then with the use of the Wheeler assumption for $\dot{z}'$ and $\dot{\rho}'$ [13], and converting the sums to integrals, one obtains

$$\sum_{i,j} m_i m_j \dot{\mathbf{r}}'_i\dot{\mathbf{r}}'_j = \sigma_m^2\left[\int_{vol}\dot{z}'\mathrm{d}^3r\right]^2. \tag{23}$$

After the use of Leibnitz formula, one obtains

$$\int_{vol}\dot{z}'\mathrm{d}^3r = \pi\left\{\sum_k\left[\int_{z_m}^{z_M}\rho_s^2(z)X_k(z)\mathrm{d}z\right]\dot{q}_k\right\} \tag{24}$$

and as a consequence one has the correction term due to the center-of-mass motion for every component kk' of the mass tensor:

$$B^c_{kk'} = \frac{\sigma_m^2\pi^2}{M}\left\{\left[\int_{z_m}^{z_M}\rho_s^2(z)X_k(z)\mathrm{d}z\right] \times\left[\int_{z_m}^{z_M}\rho_s^2(z')X_{k'}(z')\mathrm{d}z'\right]\right\}, \quad (25)$$

where σ_m^2 is the uniform mass density and M is the total mass. Finally, the components of the inertia are calculated as

$$B_{kk'} = B'_{kk'} - B^c_{kk'}. \quad (26)$$

The set of functions (7) permits to contract the tensor along R-direction. It is possible now to write the total mass inertia in a complete form:

$$\begin{aligned}B(R) = {} & B_{b_Pb_P}\left(\frac{\mathrm{d}b_P}{\mathrm{d}R}\right)^2 + 2B_{b_P\chi_T}\frac{\mathrm{d}b_P}{\mathrm{d}R}\frac{\mathrm{d}\chi_T}{\mathrm{d}R} \\ & +2B_{b_P\chi_P}\frac{\mathrm{d}b_P}{\mathrm{d}R}\frac{\mathrm{d}\chi_P}{\mathrm{d}R}+2B_{b_PR}\frac{\mathrm{d}b_P}{\mathrm{d}R}+B_{\chi_T\chi_T}\left(\frac{\mathrm{d}\chi_T}{\mathrm{d}R}\right)^2 \\ & +2B_{\chi_T\chi_P}\frac{\mathrm{d}\chi_T}{\mathrm{d}R}\frac{\mathrm{d}\chi_P}{\mathrm{d}R} + 2B_{\chi_TR}\frac{\mathrm{d}\chi_T}{\mathrm{d}R} \\ & +B_{\chi_P\chi_P}\left(\frac{\mathrm{d}\chi_P}{\mathrm{d}R}\right)^2 + 2B_{\chi_PR}\frac{\mathrm{d}\chi_P}{\mathrm{d}R} + B_{RR}. \quad (27)\end{aligned}$$

At this point one has to emphasize that the laws of variation (3), (4) and (5) restrict by no means the freedom of the system to follow any fusion path. The final dynamical trajectory in the multidimensional space is the result of minimization over all possible values (b_P, χ_T, χ_P, R), which corresponds to browsing the whole range of $(\kappa_T, \kappa_P, i_P)$ in any direction at a fixed R. The usual WKB penetrability P is calculated as

$$P = \exp(-K_{ov}), \quad (28)$$

where K_{ov} is the overlapping action integral. The tunneling energy is considered at the level of the ground state of the compound nucleus. K_{ov} reads

$$K_{ov}(b_P, \kappa_T, \kappa_P; R) = \frac{2}{\hbar}\int_{(fus)}[2B(R)_{b_P,\kappa_T,\kappa_P}E_{def}(R)_{b_P,\kappa_T,\kappa_P}]^{1/2}\mathrm{d}R. \quad (29)$$

In this way K_{ov} has a local point value in the space of (b_P, χ_T, χ_P, R), along which numerical multidimensional minimization is performed, and the final sub-barrier fusion path is obtained. The numerical procedure involves the construction of the multidimensional grid along the distance between centers. One calculates the minimum of the integrand step by step, by suming all the previous values starting from the entrance point in the barrier up to every hyperplane at a given R-value. At the next step, $R + \Delta R$, the added term accounts for all point values of $E_{def}B$, and the minimum sum is retained. At the end, one obtains a sequence of shapes through (b_P, χ_T, χ_P) along R, which is in fact the fusion path [14].

4 Results and discussion

The algorithm has been applied to the synthesis of $^{294,290,286,280}118$ nuclei. For every superheavy system the entire possible range of mass asymmetry has been taken into account. Target-projectile pairs start from symmetry $\eta_A = 0$ ($A_T \simeq A_P$) up to the asymmetry value, where there is still the possibility to have a stable target (a few tens of minutes halflife). For superheavy production, especially in the neutron-rich region like $^{294}118$, there is always the problem of having both partners between the drip lines. One has to stress that most of the reactions used in this work are most likely to be obtained only with the help of radioactive beams, since due to the large necessary neutron number, for certain mass asymmetries it is impossible to have both partners around the stability line. Once the static barriers are obtained from the minima on the potential energy surface, the mass asymmetry is completed with finding the charge asymmetry, by repeating the calculations for all possible (Z_T, Z_P) for the same (A_T, A_P). At the end the mass tensor and penetrability are calculated for all (A_T, Z_T)-(A_P, Z_P) reaction channels by preserving R as the main free variable. The target-projectile pairs with the best chances to synthesize the final superheavy system by tunneling at the ground-state energy level are chosen for presentation for everyone of the four final isotopes.

4.1 $^{294}118$

As the result of static multidimensional minimization in the (b_P, χ_T, χ_P) space along R, the first potential energy surface (PES) has been obtained for the neutron-rich superheavy system $^{294}118$ in fig. 3, as a function of the reduced distance between centers $R - R_f$ and the mass asymmetry $\eta_A = (A_T - A_P)/A$. Two maxima appear between symmetric reactions and $\eta_A \simeq 0.15$, both of them

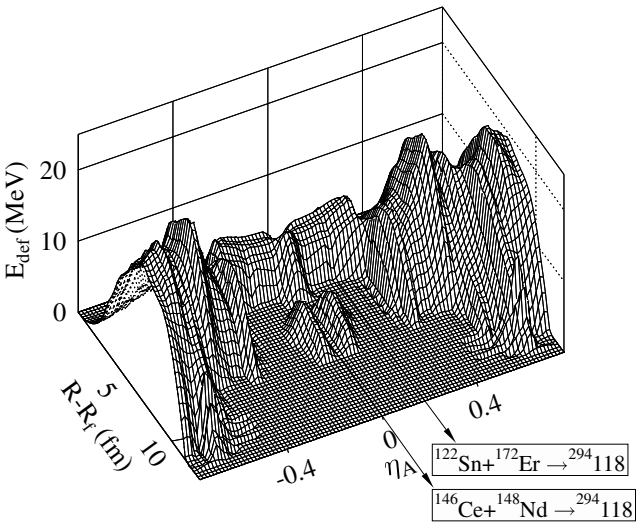

Fig. 3. Potential energy surface of $^{294}118$ as a function of fusion reaction mass asymmetry η_A and distance between centers R, after static minimization over (b_P, χ_T, χ_P).

Table 1. Dynamic barriers and penetrabilities for the synthesis of $^{294}118$.

Reaction	E_b (MeV)	$\log_{10} P$	Reaction	E_b (MeV)	$\log_{10} P$
$^{146}\mathrm{Ce}+^{148}\mathrm{Nd}$	7.5	−8.27	$^{126}\mathrm{Te}+^{168}\mathrm{Dy}$	8.	−7.77
$^{146}\mathrm{Nd}+^{148}\mathrm{Ce}$	7.2	−7.74	$^{124}\mathrm{Sn}+^{170}\mathrm{Er}$	7.7	−7.59
$^{144}\mathrm{Ce}+^{150}\mathrm{Nd}$	6.95	−7.35	$^{124}\mathrm{Cd}+^{170}\mathrm{Yb}$	7.05	−6.98
$^{144}\mathrm{Ba}+^{150}\mathrm{Sm}$	6.51	−7.29	$^{122}\mathrm{Sn}+^{172}\mathrm{Er}$	6.99	−7.05
$^{142}\mathrm{Ce}+^{152}\mathrm{Nd}$	6.15	−13.54	$^{122}\mathrm{Cd}+^{172}\mathrm{Yb}$	7.11	−8.38
$^{142}\mathrm{Ba}+^{152}\mathrm{Sm}$	6.81	−7.19	$^{120}\mathrm{Sn}+^{174}\mathrm{Er}$	8.72	−8.55
$^{140}\mathrm{Ba}+^{154}\mathrm{Sm}$	6.56	−6.85	$^{120}\mathrm{Cd}+^{174}\mathrm{Yb}$	7.19	−9.46
$^{138}\mathrm{Ba}+^{156}\mathrm{Sm}$	5.91	−10.11	$^{118}\mathrm{Cd}+^{176}\mathrm{Yb}$	6.67	−6.55
$^{138}\mathrm{Xe}+^{156}\mathrm{Gd}$	6.4	−6.11	$^{118}\mathrm{Pd}+^{176}\mathrm{Hf}$	7.57	−7.59
$^{136}\mathrm{Te}+^{158}\mathrm{Dy}$	6.24	−5.97	$^{116}\mathrm{Cd}+^{178}\mathrm{Yb}$	8.69	−8.95
$^{136}\mathrm{Xe}+^{158}\mathrm{Gd}$	6.67	−6.38	$^{116}\mathrm{Pd}+^{178}\mathrm{Hf}$	7.89	−8.1
$^{134}\mathrm{Xe}+^{160}\mathrm{Gd}$	6.3	−7.53	$^{114}\mathrm{Pd}+^{180}\mathrm{Hf}$	7.55	−7.75
$^{134}\mathrm{Te}+^{160}\mathrm{Dy}$	6.56	−6.24	$^{114}\mathrm{Cd}+^{180}\mathrm{Yb}$	8.26	−13.91
$^{132}\mathrm{Sn}+^{162}\mathrm{Er}$	6.34	−6.08	$^{112}\mathrm{Pd}+^{182}\mathrm{Hf}$	8.71	−9.53
$^{132}\mathrm{Te}+^{162}\mathrm{Dy}$	6.81	−6.6	$^{112}\mathrm{Ru}+^{182}\mathrm{W}$	7.88	−8.44
$^{132}\mathrm{Xe}+^{162}\mathrm{Gd}$	7.28	−7.12	$^{110}\mathrm{Ru}+^{184}\mathrm{W}$	7.89	−8.74
$^{130}\mathrm{Te}+^{164}\mathrm{Dy}$	6.51	−6.47	$^{110}\mathrm{Pd}+^{184}\mathrm{Hf}$	8.05	−14.2
$^{130}\mathrm{Sn}+^{164}\mathrm{Er}$	6.58	−6.44	$^{108}\mathrm{Ru}+^{186}\mathrm{W}$	7.98	−14.19
$^{128}\mathrm{Te}+^{166}\mathrm{Dy}$	7.55	−7.34	$^{108}\mathrm{Mo}+^{186}\mathrm{Os}$	7.32	−13.45
$^{128}\mathrm{Sn}+^{166}\mathrm{Er}$	6.93	−6.82	$^{106}\mathrm{Mo}+^{188}\mathrm{Os}$	8.31	−14.61
$^{126}\mathrm{Sn}+^{168}\mathrm{Er}$	6.67	−6.55	$^{106}\mathrm{Ru}+^{188}\mathrm{W}$	8.69	−15.2

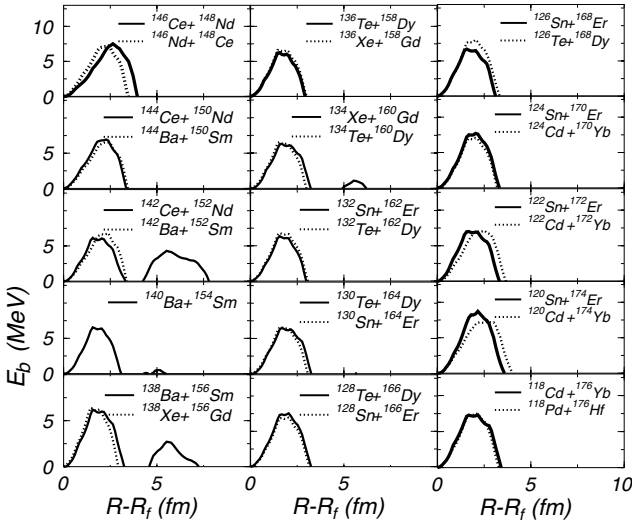

Fig. 4. Cold fusion barriers for isobaric reactions laying within the quasi-symmetric valley of $^{294}118$.

lower than any other energy height for larger mass asymmetry. Between $\eta_A \simeq 0.15$ and 0.35, the fusion barriers are characterized by a very deep entrance point, which corresponds to a high degree of overlapping between the target and the projectile within the fusion-like shape configuration. For $\eta_A > 0.35$ barriers become much wider. After a narrow valley up to $\eta_A \simeq 0.4$, the heights drastically increase, as well as the widths. Obviously, for $\eta_A > 0.35$, cold fusion reactions leading to the synthesis of $^{294}118$ are of no interest. Two out of the possible reactions are marked on the figure: the symmetric one with ^{146}Ce as a projectile and proton magic projectile ^{122}Sn-reaction. The next step consists in the calculation of all possible isobaric reactions within the range of interest for η_A, hence for every mass asymmetry one shall move in η_Z-direction. The corresponding cold fusion barriers are displayed in fig. 4. Reaction partners have been chosen with respect to two criteria: 1) both nuclei, but especially the heavy one (target) should have the largest possible lifetime; it is very difficult to find two stable systems due to the large neutron number, consequently they have been chosen as to have at least tens of minutes in halflife; 2) the reactions with the highest penetrability among those with the same η_A are displayed. One can see that barriers usually have only one maximum. The first three isobaric sets, closest to symmetry, contain spheroidally deformed target and projectile. Starting with ^{140}Ba, almost all projectiles are spherical, and targets are deformed. The only exceptions are ^{122}Cd and ^{120}Cd. Table 1 presents the numerical results about all possible, relatively stable cold fusion reactions towards the synthesis of $^{294}118$. Although the differences in barrier height E_b are small, penetrabilities $\log P$ have a large range of variation. The $Z = 50$ proton closure has an important influence. ^{136}Te, ^{126,132}Sn and ^{118}Cd, though not with the lowest barriers, have the highest calculated penetrabilities.

4.2 $^{290}118$

Four neutrons less, $^{290}118$ displayes a PES without the pronounced ridge at symmetry (see fig. 5). This superheavy nucleus is calculated as spherical. The lowest barrier height has been computed for $^{144}\mathrm{Ce}+^{146}\mathrm{Nd}$. As mass

Table 2. Dynamic barriers and penetrabilities for the synthesis of $^{290}118$.

Reaction	E_b (MeV)	$\log_{10} P$	Reaction	E_b (MeV)	$\log_{10} P$
$^{144}Ce + ^{146}Nd$	4.4	−5.	$^{128}Sn + ^{162}Er$	5.21	−4.31
$^{144}Nd + ^{146}Ce$	4.56	−5.89	$^{126}Te + ^{164}Dy$	5.87	−5.32
$^{142}Ce + ^{148}Nd$	4.47	−4.51	$^{126}Sn + ^{164}Er$	5.48	−4.81
$^{142}Ba + ^{148}Sm$	4.2	−4.52	$^{124}Sn + ^{166}Er$	4.96	−4.64
$^{140}Ce + ^{150}Nd$	4.35	−4.91	$^{124}Te + ^{166}Dy$	6.37	−5.68
$^{140}Ba + ^{150}Sm$	4.5	−4.17	$^{122}Sn + ^{168}Er$	6.12	−5.5
$^{138}Ba + ^{152}Sm$	4.86	−4.42	$^{122}Cd + ^{168}Yb$	5.07	−5.39
$^{138}Xe + ^{152}Gd$	4.4	−4.04	$^{120}Sn + ^{170}Er$	5.69	−7.67
$^{136}Ba + ^{154}Sm$	4.44	−4.33	$^{120}Cd + ^{170}Yb$	5.04	−6.03
$^{136}Xe + ^{154}Gd$	4.66	−4.33	$^{118}Sn + ^{172}Er$	6.37	−5.68
$^{134}Ba + ^{156}Sm$	5.58	−5.02	$^{116}Cd + ^{174}Yb$	5.88	−5.35
$^{134}Xe + ^{156}Gd$	5.13	−4.61	$^{116}Pd + ^{174}Hf$	5.19	−4.6
$^{132}Xe + ^{158}Gd$	4.57	−4.31	$^{114}Cd + ^{176}Yb$	5.54	−7.94
$^{132}Te + ^{158}Dy$	4.98	−4.49	$^{114}Pd + ^{176}Hf$	6.31	−5.9
$^{130}Xe + ^{160}Gd$	5.77	−5.19	$^{112}Pd + ^{178}Hf$	6.05	−5.51
$^{130}Te + ^{160}Dy$	5.29	−4.76	$^{112}Cd + ^{178}Yb$	6.	−8.88
$^{128}Te + ^{162}Dy$	4.77	−4.44	$^{110}Cd + ^{180}Yb$	6.33	−10.38
$^{128}Xe + ^{162}Gd$	5.91	−6.27			

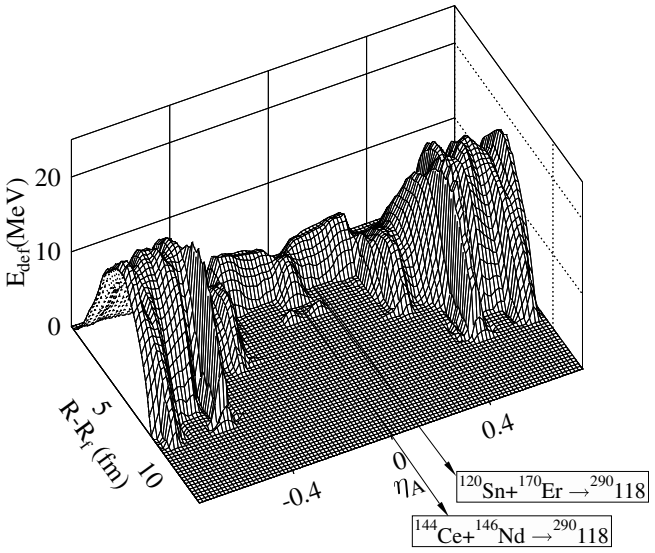

Fig. 5. Potential energy surface of $^{290}118$ as a function of fusion reaction mass asymmetry η_A and distance between centers R, after static minimization over (b_P, χ_T, χ_P).

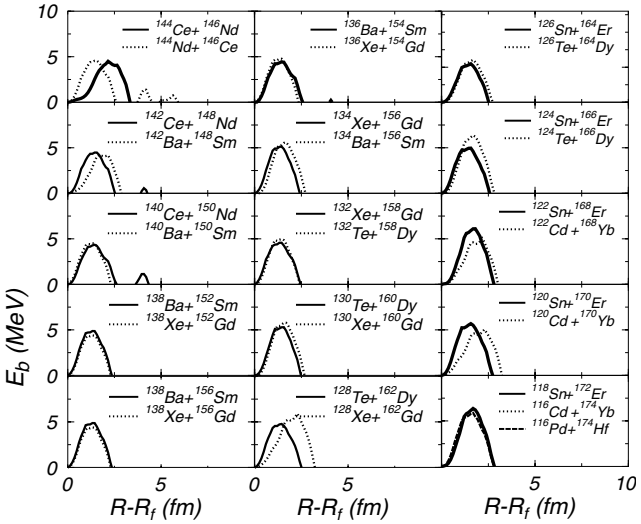

Fig. 6. Cold fusion barriers for isobaric reactions laying within the quasi-symmetric valley of $^{290}118$.

asymmetry increases, the entrance point is more advanced and barriers are very narrow, but slightly higher. At $\eta_A \simeq 0.25$, barriers suddenly increase their width. It is the point where projectiles distance themselves from $Z = 50$ with more than four protons. For $\eta_A > 0.25$ barriers become very large and high. The result of isobaric reaction search within $\eta_A \in (0,\ 0.25)$ is firstly presented in fig. 6, as being the cold fusion barriers for the highest calculated penetrabilities. As a general observation, barrier heights are lower and narrower than for $^{294}118$. Again the most part of the reactions have a spherical projectile. Also the proton-richer projectile reaction has a larger width within the isobaric set. Differences are analyzed now with respect to the results from table 2, where the heights E_b of the dynamic barriers and penetrabilities $\log P$ are presented. One notices that penetrabilities are 2–3 orders of magnitude higher than in the previous case. ^{140}Ba and ^{138}Xe projectile reactions have the highest chance for tunneling. These reactions belong to the fusion channels with quasi-symmetric masses. Both projectiles are spherical, both targets, ^{150}Sm ($\beta_2 = 0.206$, $\chi_T = 0.755$) and ^{152}Gd ($\beta_2 = 0.207$, $\chi_T = 0.754$) are deformed. Among the more asymmetric reactions, ^{128}Sn and ^{116}Pd, though not with the lowest barriers, have rather high penetrabilities: $\log P = -4.31$ and -4.6, respectively.

Table 3. Dynamic barriers and penetrabilities for the synthesis of $^{286}118$.

Reaction	E_b (MeV)	$\log_{10} P$	Reaction	E_b (MeV)	$\log_{10} P$
^{142}Ce + ^{144}Nd	4.3	−3.48	**^{128}Sn + ^{158}Er**	**3.2**	**−2.56**
^{142}Nd + ^{144}Ce	3.85	−3.53	^{128}Xe + ^{158}Gd	5.48	−5.82
^{140}Ce + ^{146}Nd	3.7	−3.7	^{128}Te + ^{158}Dy	4.85	−4.22
^{140}Nd + ^{146}Ce	4.1	−3.4	^{126}Xe + ^{160}Gd	5.44	−6.58
^{140}Ba + ^{146}Sm	4.19	−8.71	^{126}Te + ^{160}Dy	4.02	−3.33
^{138}Ce + ^{148}Nd	4.06	−3.35	**^{126}Sn + ^{160}Er**	**3.51**	**−2.9**
^{138}Ba + ^{148}Sm	3.54	−2.83	^{124}Sn + ^{162}Er	5.2	−4.55
^{136}Ba + ^{150}Sm	3.92	−3.39	^{124}Te + ^{162}Dy	4.44	−3.65
^{136}Ce + ^{150}Nd	5.54	−4.86	^{122}Te + ^{164}Dy	4.82	−3.93
^{136}Xe + ^{150}Gd	3.37	−2.69	^{122}Sn + ^{164}Er	4.27	−3.47
^{134}Ba + ^{152}Sm	4.23	−3.49	^{120}Te + ^{166}Dy	5.14	−4.28
^{134}Xe + ^{152}Gd	3.71	−3.06	^{120}Sn + ^{166}Er	4.59	−3.75
^{132}Ba + ^{154}Sm	5.6	−5.55	^{118}Sn + ^{168}Er	4.98	−4.11
^{132}Xe + ^{154}Gd	4.18	−3.63	**^{118}Cd + ^{168}Yb**	**4.37**	**−3.6**
^{132}Te + ^{154}Dy	**3.02**	**−2.4**	^{116}Sn + ^{170}Er	5.42	−4.5
^{130}Ba + ^{156}Sm	5.52	−6.25	^{116}Cd + ^{170}Yb	4.8	−3.93
^{130}Xe + ^{156}Gd	3.79	−3.18	^{116}Pd + ^{170}Hf	5.08	−4.6
^{130}Te + ^{156}Dy	3.34	−2.71	^{114}Sn + ^{172}Er	5.87	−5.27

4.3 ^{286}118

The potential energy surface for ^{286}118 is displayed if fig. 7. The deformation for this compound superheavy nucleus is taken as $\beta_2 = 0.08$ which corresponds to $\chi(^{286}118) = 0.89$, hence a deformed system. Potential heights are lower than in the two previous cases. Energy valleys are visible especially around symmetrical reactions. Deeper barrier entrance points cover the range of η_A between symmetry and 0.3. The lowest barriers stand for $\eta_A \in [0, 0.1]$. Two possible cold fusion channels, the symmetric ^{142}Ce + ^{144}Nd and asymmetric ^{118}Sn + ^{168}Ce are marked on the figure. The barriers obtained as the result of multidimensional minimization, are presented in fig. 8. The isobaric sets have been chosen as those with the largest lifetimes for the partners and especially for the target nuclei. Heights below 5 MeV are the most common. The shift of energy maxima towards a more elongated shape are obvious for reactions with proton-richer projectiles and $A_T + A_P = 142 + 144$ and 140 + 146. Narrow and low barriers are common to spherical projectiles. It is a characteristic feature of these barriers to have the largest and higher dynamical cold fusion barriers for deformed projectiles. Such examples are ^{136}Ce + ^{150}Nd, ^{132}Ba + ^{154}Sm, ^{130}Ba + ^{156}Sm, ^{128}Xe + ^{158}Gd and ^{126}Xe + ^{160}Gd, where all the light nuclei (projectiles) are spheroidally deformed. All the rest of the reactions have spherical projectiles.

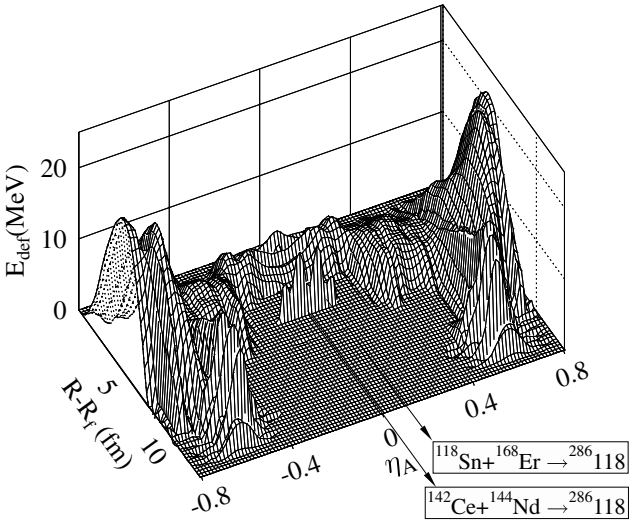

Fig. 7. Potential energy surface of ^{286}118 as a function of η_A and R, after static minimization over (b_P, η_T, η_P).

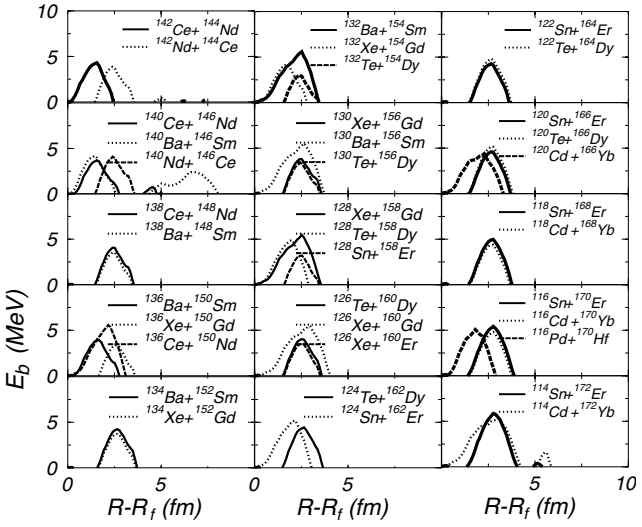

Fig. 8. Cold fusion barriers for isobaric fusion channels within the asymmetric energy valley $\eta_A \simeq 0.3$ of ^{286}118.

In table 3 the result of multidimensional minimization of the action integral is presented for the synthesis of $^{286}118$ along the cold fusion channels in the range of mass asymmetry $\eta_A = [0, 0.3]$. The lowest penetrability values are produced by the deformed projectile reactions. The highest values of $\log P$ are obtained for spherical ^{136}Xe, ^{130,132}Te and ^{126,128}Sn projectiles. $Z = 50$ proton closure plays an important role in $^{128}\mathrm{Sn} + {}^{158}\mathrm{Er}$ ($\log P = -2.56$) and $^{126}\mathrm{Sn} + {}^{160}\mathrm{Er}$ ($\log P = -2.9$) reactions, since the negative shell corrections energy of the projectiles influence the widths of the barriers as long as microscopic individuality is preserved. Another observation is that among the same isobaric set, the neutron-richer projectile has the best chances (highest $\log P$) to form the superheavy nucleus by tunneling. The ^{136}Xe-projectile reaction has a higher penetrability ($\log P = -2.69$) than the ^{136}Ba-projectile one ($\log P = -3.39$), which is in turn more favoured than the ^{136}Ce-projectile one ($\log P = -4.86$).

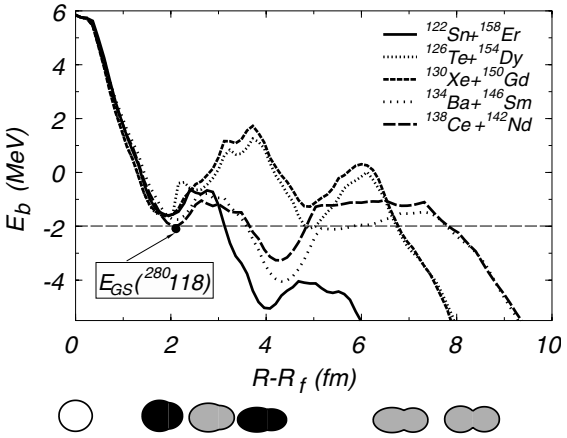

Fig. 10. The lowest barriers for the synthesis of $^{280}118$ and the deformed ground-state energy. Below are the shape configurations for ground state, minimum and entrance points.

4.4 $^{280}118$

The last superheavy nucleus analyzed in this work is the neutron poor $^{280}118$. A special mention concerns the possible deformed neutron closure $N = 162$ [15]. This neutron shell could stabilize the system more than the other $Z = 118$ isotopes. At least to our knowledge, there are no calculations concerning the ground-state deformation of this nucleus. Thus, the first step in the approach is to find out such a local energy minimum within the space of deformation of (b_P, χ_T, χ_P, R). Calculations have been performed starting with the hypothesis of a spherical $^{280}118$. After minimization along R in b_P, χ_T, χ_P directions, the potential energy surface presented in fig. 9 has been obtained. The first observation on the figure is that this superheavy nucleus is deformed. The spherical state, at $R - R_f = 0$ is at a higher energy than for a larger distance between centers. The surface goes down to $R - R_f \simeq 2$ fm. Then, a local pocket around symmetric reactions is visible, within the prolongation of the $^{138}\mathrm{Ce} + {}^{142}\mathrm{Nd}$ channel, marked on the figure. The pocket stretch up to $\eta_A \simeq 0.2$. This region shall be browsed furtheron. A projection of the lowest barriers E_b within this range of mass asymmetry on the $R - R_f$-direction is presented in fig. 10. The spherical state lies at $R - R_f = 0$ and is marked by the white circle below the scale. Then a first minimum appears for all barriers. The one from $^{138}\mathrm{Ce} + {}^{142}\mathrm{Nd}$ distinguishes as the lowest. It is this point which shall be considered as the ground-state deformation energy E_{GS}. Its corresponding shape has been drawn below in black. In order to obtain all the cold fusion barriers for $^{280}118$, $E_{GS} = 2.1$ MeV is subtracted from all deformation energies along R. A peculiarity of the barriers displayed in fig. 10 is the presence of a second minimum at about $R - R_f \simeq 4$ fm. The deepest one belongs to $^{122}\mathrm{Sn} + {}^{158}\mathrm{Er}$ reaction, and the corresponding configuration is drawn as a black shape. Such minima can accomodate rotating shape isomers, especially in low-energy reactions. The dark grey shapes represent the barrier entrance point configuration for (from left to right) $^{122}\mathrm{Sn} + {}^{158}\mathrm{Er}$, $^{126}\mathrm{Te} + {}^{154}\mathrm{Dy}$ and $^{138}\mathrm{Ce} + {}^{142}\mathrm{Nd}$, respectively. The result of scaling to E_{GS} is presented in fig. 11. The symmetric reactions $(138 + 142)$ have flat but large barriers. One has to mention that calculations have been made so that when the binary system reaches $R - R_f = 2$ fm (the distance where the ground-state minimum has been found), the binary configuration moves on in η_A-direction, a situation also analyzed and predicted in [5]. Again the largest and highest barriers are produced by deformed projectiles. Ce-projectiles are all spheroidally deformed, as well as ^{122,124,126}Xe projectiles. When the xenon isotope is spherical, it displays a very low and narrow barrier, like ^{132,134}Xe-reactions. The corresponding barrier heights and $\log P$-values are presented in table 4. First mention is that penetrabilities are many orders of magnitude higher than those obtained for the synthesis of the previous isotopes. $^{138}\mathrm{Ba} + {}^{142}\mathrm{Sm}$ and $^{134}\mathrm{Xe} + {}^{146}\mathrm{Gd}$, both with spherical

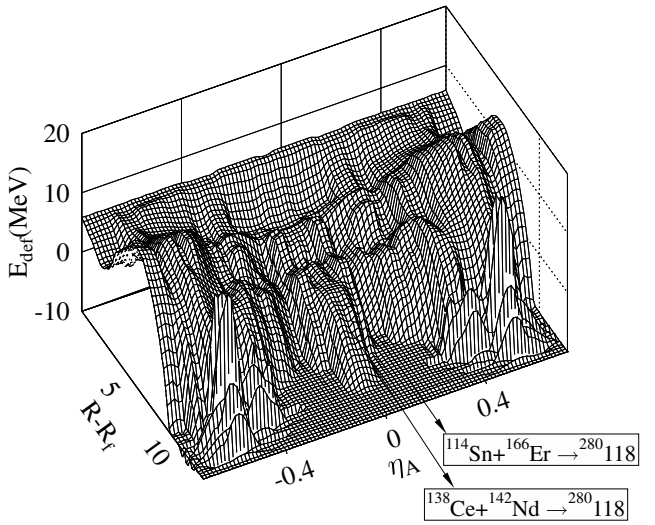

Fig. 9. Potential energy surface of $^{280}118$ as a function of η_A and R, after static minimization over (b_P, η_T, η_P), unscaled to the ground-state energy.

Table 4. Dynamic barriers and penetrabilities for the synthesis of $^{280}118$.

Reaction	E_b (MeV)	$\log_{10} P$	Reaction	E_b (MeV)	$\log_{10} P$
$^{138}\mathrm{Nd}+^{142}\mathrm{Ce}$	1.48	−5.22	$^{126}\mathrm{Xe}+^{154}\mathrm{Gd}$	3.29	−3.32
$^{138}\mathrm{Ce}+^{142}\mathrm{Nd}$	0.95	−3.94	$^{126}\mathrm{Te}+^{154}\mathrm{Dy}$	3.24	−6.72
$^{138}\mathbf{Ba}+^{142}\mathbf{Sm}$	**0.39**	**−0.59**	$^{124}\mathrm{Xe}+^{156}\mathrm{Gd}$	3.67	−3.79
$^{136}\mathrm{Ce}+^{144}\mathrm{Nd}$	3.81	−3.31	$^{124}\mathrm{Te}+^{156}\mathrm{Dy}$	2.01	−1.9
$^{136}\mathrm{Ba}+^{144}\mathrm{Sm}$	1.61	−1.91	$^{124}\mathrm{Sn}+^{156}\mathrm{Er}$	1.17	−1.15
$^{134}\mathrm{Ce}+^{146}\mathrm{Nd}$	3.54	−3.56	$^{122}\mathrm{Xe}+^{158}\mathrm{Gd}$	4.28	−4.34
$^{134}\mathrm{Ba}+^{146}\mathrm{Sm}$	1.2	−2.4	$^{122}\mathrm{Te}+^{158}\mathrm{Dy}$	3.29	−3.32
$^{134}\mathrm{Xe}+^{146}\mathrm{Gd}$	0.81	−0.77	$^{122}\mathrm{Sn}+^{158}\mathrm{Er}$	1.32	−1.31
$^{132}\mathrm{Ce}+^{148}\mathrm{Nd}$	3.9	−3.81	$^{120}\mathrm{Xe}+^{160}\mathrm{Gd}$	4.63	−5.37
$^{132}\mathrm{Ba}+^{148}\mathrm{Sm}$	2.88	−3.09	$^{120}\mathrm{Te}+^{160}\mathrm{Dy}$	3.13	−3.43
$^{132}\mathrm{Xe}+^{148}\mathrm{Gd}$	1.69	−1.58	$^{120}\mathbf{Sn}+^{160}\mathbf{Er}$	**1.31**	**−1.86**
$^{130}\mathrm{Ce}+^{150}\mathrm{Nd}$	4.07	−4.32	$^{118}\mathrm{Te}+^{162}\mathrm{Dy}$	2.95	−2.83
$^{130}\mathrm{Ba}+^{150}\mathrm{Sm}$	3.34	−3.28	$^{118}\mathrm{Sn}+^{162}\mathrm{Er}$	2.32	−2.07
$^{130}\mathbf{Xe}+^{150}\mathbf{Gd}$	**3.71**	**−7.87**	$^{118}\mathbf{Cd}+^{162}\mathbf{Yb}$	**1.68**	**−1.57**
$^{128}\mathrm{Ba}+^{152}\mathrm{Sm}$	3.8	−3.7	$^{116}\mathrm{Sn}+^{164}\mathrm{Er}$	2.66	−2.53
$^{128}\mathrm{Xe}+^{152}\mathrm{Gd}$	2.82	−3.	$^{116}\mathrm{Cd}+^{164}\mathrm{Yb}$	1.99	−2.04
$^{126}\mathrm{Ba}+^{154}\mathrm{Sm}$	4.28	−4.34			

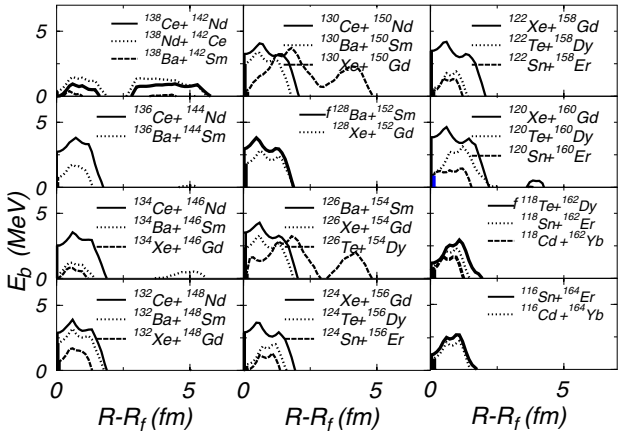

Fig. 11. Cold fusion barriers for isobaric fusion channels within the asymmetric energy valley $\eta_A \simeq 0.3$ of $^{280}118$.

projectiles, are two promising reactions for sub-barriers fusion towards synthesis of $^{280}118$. Barrier height is an important parameter, but not decisive. $^{138}\mathrm{Ce}+^{142}\mathrm{Nd}$ has a low barrier, but due to its width its penetrability is rather low ($\log P = -3.94$). Another reason is the influence of the couplings between different degrees of freedom, which manifest themselves through the mass tensor components. The couplings can drive the system towards even higher-energy values than the minimum energy path, provided the action integral takes lower values. Other remarkable reactions are $^{124}\mathrm{Te}+^{156}\mathrm{Dy}$ ($\log P = -1.9$), $^{124}\mathrm{Sn}+^{156}\mathrm{Er}$ ($\log P = -1.15$), $^{122}\mathrm{Sn}+^{158}\mathrm{Dy}$ ($\log P = -1.31$) and $^{118}\mathrm{Cd}+^{162}\mathrm{Yb}$ ($\log P = -1.57$). All the projectiles for these reactions are spherical and targets are deformed. One can emphasize that $^{280}118$ superheavy system has the best chances to be synthesized by tunneling through cold fusion reactions. The favoured channels are found around symmetric masses of target and projectile.

5 Conclusions

A binary configuration model has been used within a large number of degrees of freedom to calculate the barriers and penetrabilties towards the synthesis of $^{294,290,286,280}118$ superheavy isotopes. Dynamical multidimensional minimization of the action integral yielded the penetrabilities by WKB method. The barriers are larger and higher, and penetrabilities are lower as the system is neutron richer. The highest $\log P$ for every superheavy isotope are calculated for spherical projectiles. Also, among isobaric sets of reactions, the neutron-richer projectile generates the highest penetrability. $^{286}118$ and $^{280}118$ are the most appropriated isotopes to be produced by tunneling, at a kinetic energy equal to the Q-value of the reaction. $^{132}\mathrm{Te}+^{154}\mathrm{Dy}$ and $^{128}\mathrm{Sn}+^{158}\mathrm{Er}$ for $^{286}118$ and $^{138}\mathrm{Ba}+^{142}\mathrm{Sm}$, $^{134}\mathrm{Xe}+^{146}\mathrm{Gd}$, $^{124}\mathrm{Sn}+^{156}\mathrm{Er}$ and $^{122}\mathrm{Sn}+^{158}\mathrm{Er}$ channels for $^{280}118$ have been calculated as having the highest penetrabilty values, hence the best chances to reach the synthesis of superheavy nuclei by sub-barrier reaction.

References

1. S. Hofmann, G. Münzenberg, Rev. Mod. Phys. **72**, 733 (2000).
2. M. Bender, K. Rutz, P-G. Reinhard, J.A. Maruhn, W. Greiner, Phys. Rev. C **58**, 2126 (1998).
3. J.F. Berger *et al.*, Nucl. Phys. A **685**, 1 (2001).
4. M. Goncalves, S.B. Duarte, Phys. Rev. C **48**, 2409 (1993).
5. G.G. Adamian, N.V. Antonenko, W. Scheid, Phys. Rev. C **68**, 034601 (2003).
6. R.A. Gherghescu, Phys. Rev. C **67**, 014309 (2003).
7. V. Strutinsky, Nucl. Phys. A **95**, 420 (1967).
8. A. Sobiczewski, Phys. Part. Nucl. **25**, 295 (1994).
9. K.T. Davies, A.J. Sierk, J. Comput. Phys. **18**, 311 (1975).

10. H.J. Krappe, J.R. Nix, A.J. Sierk, Phys. Rev. C **20**, 992 (1979).
11. R.A. Gherghescu, W. Greiner, Phys. Rev. C **68**, 044314 (2003).
12. D.N. Poenaru, M. Ivascu, D. Mazilu, Comput. Phys. Commun. **19**, 205 (1980).
13. K.T. Davies, A.J. Sierk, J.R. Nix, Phys. Rev. C **13**, 2385 (1976).
14. R.A. Gherghescu, J. Skalski, Z. Patyk, A. Sobiczewski, Nucl. Phys. A **651**, 237 (1999).
15. S. Cwiok, V.V. Pashkevich, J. Dudek, W. Nazarewicz, Nucl. Phys. A **410**, 254 (1983).